J. Fluid Mech. (2010), *vol.* 647, *pp.* 105–124.
doi:10.1017/S002211200999396X

Onset of convection in two layers of a binary liquid

G. B. McFADDEN†, S. R. CORIELL AND P. A. LOTT

National Institute of Standards and Technology, Gaithersburg, MD 20899, USA

(Received 24 August 2009; revised 23 November 2009; accepted 11 December 2009)

We perform linear stability calculations for horizontal bilayers of a two-component fluid that can undergo a phase transformation, taking into account both buoyancy effects and thermocapillary effects in the presence of a vertical temperature gradient. Critical values for the applied temperature difference across the system that is necessary to produce instability are obtained by a linear stability analysis, using both numerical computations and small wavenumber approximations. Thermophysical properties are taken from the aluminum–indium monotectic system, which includes a liquid–liquid miscibility gap. In addition to buoyant and thermocapillary modes of instability, we find an oscillatory phase-change instability due to the combined effects of solute diffusion and fluid flow that persists at small wavenumbers. This mode is sensitive to the ratio of the layer depths, and for certain layer depths can occur for heating from either above or below.

1. Introduction

Materials science provides a rich source of interfacial instabilities driven by convective heat and mass transfer (Glicksman, Coriell & McFadden 1986; Davis 1994, 2001). In this paper we consider the stability of a planar liquid–liquid interface of a binary monotectic alloy in the presence of a temperature gradient normal to the interface. The directional growth of binary monotectics can produce useful composites consisting of rod-like structures of one phase aligned in the growth direction within a second-phase matrix (Hunt & Lu 1994). Controlled growth typically takes place in a moving temperature gradient, with the higher temperature parent phase of liquid (L1) transforming at the monotectic temperature (T_M) into two daughter phases consisting of a second liquid phase (L2) and a solid phase (S). The observed geometry of the daughter phases typically consists of rods of one phase embedded in a matrix of the second phase. The resulting inter-rod spacings are often predicted using a variation (Derby & Favier 1983; Coriell *et al.* 1997; Stöcker & Ratke 1999, 2000) of the Jackson–Hunt theory (Jackson & Hunt 1966) of the related process of eutectic growth, which produces two solid phases (L $\rightarrow$ S1 + S2) instead of a solid and liquid phase (L1 $\rightarrow$ S + L2).

The Jackson–Hunt theory is less successful for predicting the spacing in monotectic alloys, and the discrepancy is often attributed to the effects of fluid flow, particularly the convection made possible by the presence of liquid–liquid (L1–L2) interfaces in the system (Hunt & Lu 1994; Stöcker & Ratke 2000). In order to study the effects of convective motion in a monotectic system theoretically we consider the simpler case of a semi-infinite stationary horizontal interface separating the two liquid phases (L1 and

† Email address for correspondence: mcfadden@nist.gov

L2) in an applied temperature gradient, while ignoring the formation of the solid phase (S). This simple geometry allows a one-dimensional base state whose linear stability can be determined in detail, either numerically or, in limiting cases, analytically. The resulting analysis of the two-layer phase-transforming system includes the effects of buoyancy, density change, capillarity and thermocapillarity.

The L1–L2 phase transition in a monotectic system is an example of a miscibility gap in a binary (two-component) material. Such miscibility gaps are very common, particularly in organic systems. The equilibrium and kinetic behaviour of systems near the critical point (T_C) of the miscibility gap, where the two phases become identical, is a subject of extensive research (Berg & Moldover 1989). In this paper we extend our previous work on single component systems (McFadden *et al.* 2007*a*,*b*; McFadden & Coriell 2009) to the case of two-component binary alloys. Specifically, we consider a metallic system, aluminum–indium, at the monotectic temperature, which is relevant for monotectic growth but is well below the critical temperature. In this system we find that in addition to the analogs of Rayleigh–Bénard modes (Turner 1973) and Marangoni modes of instability (Davis 1987) there is a novel oscillatory mode at large wavelengths that persists in the absence of either buoyancy or thermocapillarity.

The stability of a fluid–fluid interface is important in a number of scientific and technological applications. The case of non-interacting immiscible fluid bilayers has been well studied both theoretically and experimentally (Davis 1987; Joseph & Renardy 1993; Andereck *et al.* 1998; Johnson & Narayanan 1998; Schatz & Neitzel 2001; Nepomnyashchy, Verlarde & Colinet 2002; McFadden *et al.* 2007*a*). This situation can be contrasted with that of a system in which the bilayers represent different fluid phases of a given single-component material (Busse & Schubert 1971; Busse 1989; Sakurai *et al.* 1999; McFadden *et al.* 2007*b*). The phase transformation that may then occur between the two layers is described by a modification of the usual interfacial boundary conditions that are used to describe immiscible fluids. For a two-phase system there can be mass flow across the interface, which is not a material surface. In addition, latent heat is typically generated at the interface which is conducted into the surrounding fluid. Finally, a description of the thermodynamic state of the interface is required, which is often based either on an assumption of local thermodynamic equilibrium or a kinetic statement governing systematic deviations from local thermodynamic equilibrium. As a result, the stability results for a two-phase bilayer system are quantitatively and even qualitatively different than those for an immiscible system. For example, the oscillatory phase-change instability that we describe here for a binary monotectic system has no analog in immiscible systems.

The outline of the paper is as follows. In the next section we describe the model, including a summary of the thermodynamics and governing equations. Numerical results are given in § 3, followed by a summary of some small wavenumber expansions in § 4. A discussion is provided in § 5, followed by conclusions. Details about the thermophysical properties of the aluminum–indium system are given in the Appendix.

2. Model

We first describe the thermodynamic model for the aluminum–indium liquid–liquid miscibility gap (see tables 1 and 2 for thermophysical constants). We then present the governing equations and boundary conditions, and pose the linear stability problem.

Density of pure aluminum	ρ_{Al}	2.392×10^3	kg m^{-3}
Density of pure indium	ρ_{In}	6.697×10^3	kg m^{-3}
Dynamic viscosity of pure aluminum	μ_{Al}	1.322×10^{-3}	kg (s m)$^{-1}$
Dynamic viscosity of pure indium	μ_{In}	7.276×10^{-4}	kg (s m)$^{-1}$
Kinematic viscosity of pure aluminum	ν_{Al}	5.53×10^{-7}	m^2 s^{-1}
Kinematic viscosity of pure indium	ν_{In}	1.09×10^{-7}	m^2 s^{-1}
Thermal conductivity of pure aluminum	k_{Al}	0.899×10^2	J (s m K)$^{-1}$
Thermal conductivity of pure indium	k_{In}	0.482×10^2	J (s m K)$^{-1}$
Thermal diffusivity of pure aluminum	κ_{Al}	0.348×10^{-4}	m^2 s^{-1}
Thermal diffusivity of pure indium	κ_{In}	0.296×10^{-4}	m^2 s^{-1}
Partial molar volume of aluminum	$\bar{V}_{Al}$	1.003×10^{-5}	m^3 mole^{-1}
Partial molar volume of indium	$\bar{V}_{In}$	1.823×10^{-5}	m^3 mole^{-1}

TABLE 1. Thermophysical properties of pure aluminum and pure indium (Gale & Totemeier 2004) at the monotectic temperature $T_M = 909.65$ K (636.5° C).

Mole fraction of indium in the α phase	X^α	0.04657	
Mole fraction of indium in the β phase	X^β	0.8663	
Mass fraction of indium in the α phase	c^α	0.1721	
Mass fraction of indium in the β phase	c^β	0.9650	
$\mathrm{d}T/\mathrm{d}c^\alpha$	m_α	1108.0 K	
$-\mathrm{d}T/\mathrm{d}c^\beta$	m_β	4687.0 K	
Density of the α phase	ρ^α	2.689×10^3	kg m^{-3}
Density of the β phase	ρ^β	6.300×10^3	kg m^{-3}
Kinematic viscosity of the α phase	ν^α	4.536×10^{-7}	m^2 s^{-1}
Kinematic viscosity of the β phase	ν^β	1.188×10^{-7}	m^2 s^{-1}
Dynamic viscosity of the α phase	μ^α	1.220×10^{-3}	kg (s m)$^{-1}$
Dynamic viscosity of the β phase	μ^β	7.484×10^{-4}	kg (s m)$^{-1}$
Thermal expansion coefficient of the α phase	η^α	1.160×10^{-4}	K^{-1}
Thermal expansion coefficient of the β phase	η^β	1.029×10^{-4}	K^{-1}
Diffusivity of indium in aluminum in the α phase	D^α	9.0×10^{-9}	m^2 s^{-1}
Diffusivity of indium in aluminum in the β phase	D^β	9.0×10^{-9}	m^2 s^{-1}
Thermal diffusivity of the α phase	κ^α	0.339×10^{-4}	m^2 s^{-1}
Thermal diffusivity of the β phase	κ^β	0.298×10^{-4}	m^2 s^{-1}
Thermal conductivity of the α phase	k^α	0.827×10^2	J (s m K)$^{-1}$
Thermal conductivity of the β phase	k^β	0.497×10^2	J (s m K)$^{-1}$
Molar volume in the α phase	V_m^α	1.041×10^{-5}	m^3 mole^{-1}
Molar volume in the β phase	V_m^β	1.713×10^{-5}	m^3 mole^{-1}
Surface energy	γ	0.0265	J m^{-2}
Temperature dependence of surface energy	γ_T	-2.274×10^{-4}	J (K m^2)$^{-1}$
Latent heat (difference in specific enthalpy)	$L_{\alpha\beta} = h_m^\alpha - h_m^\beta$	3.099×10^5	J kg^{-1}
Total thickness of layer	d	0.01	m
Gravitational acceleration	g	9.8	m s^{-2}

TABLE 2. Thermophysical properties of the aluminum–indium system (Bräuer & Müller-Vogt 1998; Merkwitz & Hoyer 1999; Gale & Totemeier 2004) at the monotectic temperature $T_M = 909.65$ K (636.5° C).

2.1. *Thermodynamic model*

The thermodynamic equilibrium conditions for two-phase coexistence at a liquid–liquid interface can be derived from the Gibbs free energy density (Lupis 1983), $\bar{g}(T, p, c) = c\bar{\mu}_{In}(T, p, c) + (1 - c)\bar{\mu}_{Al}(T, p, c)$, where $\bar{\mu}_{Al}$ and $\bar{\mu}_{In}$ are the chemical potentials of aluminum and indium, and T, p and c are the temperature, pressure

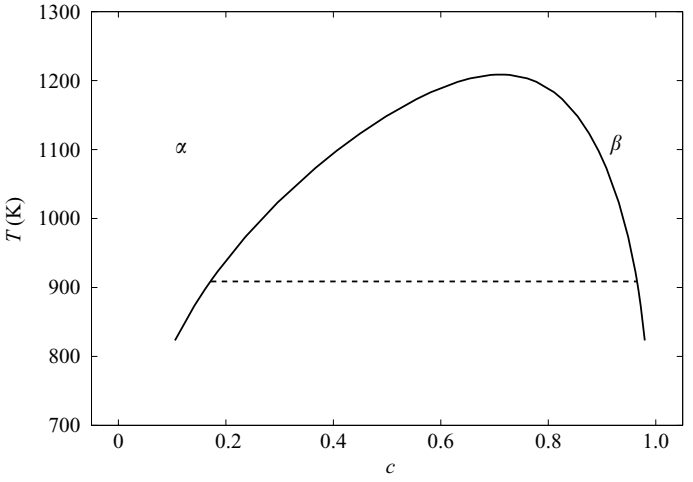

FIGURE 1. The L1–L2 coexistence curve for the thermodynamic model of the aluminum–indium system at atmospheric pressure. The dotted line at the monotectic temperature T_M connects the compositions of two-phase equilibrium. The composition c denotes the mass fraction of indium, and the α phase (β phase) is rich in aluminum (indium).

and mass fraction of indium, respectively; the mass fraction of aluminum is then $(1-c)$. If we let α and β denote the L1 (aluminum rich) and L2 (indium rich) phases, then the equilibrium mass fractions $\bar{c}^\alpha$ and $\bar{c}^\beta$ are determined from the equality of chemical potentials,

$$\bar{\mu}_{Al}(T, p, \bar{c}^\alpha) = \bar{\mu}_{Al}(T, p, \bar{c}^\beta), \quad \bar{\mu}_{In}(T, p, \bar{c}^\alpha) = \bar{\mu}_{In}(T, p, \bar{c}^\beta), \tag{2.1}$$

where T and p are the interfacial temperature and pressure. An assessment for the aluminum–indium system (Coughanowr 1989; U. R. Kattner, private communication, 2009) produced the model summarized in the Appendix. The resulting co-existence curve at atmospheric pressure p_R is shown in figure 1. At $T = T_M$ the equilibrium concentrations are given by $\bar{c}^\alpha = 0.1721$ and $\bar{c}^\beta = 0.9650$. Near these points the linearized co-existence curve takes the form

$$T = T_M + \bar{m}^\alpha (c - \bar{c}^\alpha), \quad T = T_M - \bar{m}^\beta (c - \bar{c}^\beta), \tag{2.2}$$

where $\bar{m}^\alpha > 0$ and $\bar{m}^\beta > 0$ are given in table 2, along with some additional thermophysical property values.

2.2. *Geometry and governing equations*

We consider a semi-infinite horizontal two layer system, with vertical heating across the layers. The unperturbed upper layer (the lower density α phase) extends over the interval $0 < z < \bar{H}_\alpha$, and the unperturbed lower layer (the higher density β phase) extends over the interval $-\bar{H}_\beta < z < 0$. Specifying the values of $\bar{c}^\alpha$, $\bar{c}^\beta$, $\bar{H}_\alpha$ and $\bar{H}_\beta$ determines the total amount of solute (per unit area) in the system. In the following we choose to specify the ratio $\bar{H}_\alpha / \bar{H}_\beta$, rather than specifying the total amount of solute in the system. Without loss of generality we consider linear stability results for a two-dimensional system, with velocity components u and w in the x and z directions, respectively. The perturbed interface is assumed to have the form $z = h(x, t)$; the horizontal coordinate extends over the interval $-\infty < x < \infty$. The upper boundary at $z = \bar{H}_\alpha$ and the lower boundary at $z = -\bar{H}_\beta$ are assumed to be isothermal and impermeable to solute, with no-slip boundary conditions. The equations of motion

are given by the Navier–Stokes equations in the Boussinesq approximation (Turner 1973), coupled to equations for heat and mass transfer (Landau & Lifshitz 1987).

2.3. *Base state*

We consider a quiescent one-dimensional base state with a static temperature gradient normal to the planar L1–L2 interface at $z=0$, where $T=T_M$ and $p=p_R$, with corresponding equilibrium values $\bar{c}^\alpha$ and $\bar{c}^\beta$. The solute field is assumed to be uniform in each phase, and the thermal field is

$$T^\alpha(z)=T_M+G_\alpha z \tag{2.3}$$

in the α phase, and

$$T^\beta(z)=T_M+G_\beta z \tag{2.4}$$

in the β phase. The temperature gradients in the base state satisfy

$$0=k_\alpha G_\alpha-k_\beta G_\beta, \tag{2.5}$$

where k_α and k_β are the thermal conductivities in each phase. The pressure field in the base state is hydrostatic. We assume the transport coefficients are uniform in each phase, and, following the Boussinesq approximation, we assume the density is uniform in all terms in the governing equations except for the gravitational term.

2.4. *Dimensionless parameters*

We make the equations dimensionless based on a length scale given by the total depth $d=\bar{H}_\alpha+\bar{H}_\beta$, a time scale based on the thermal time d^2/κ_β, the velocity scale κ_β/d, the temperature scale $G_\beta d$ and the pressure scale $\nu_\beta\kappa_\beta\bar{\rho}_\beta/d^2$. Here ν_β is the kinematic viscosity, κ_β is the thermal diffusivity and $\bar{\rho}_\beta=\bar{\rho}(T_M,\bar{c}^\beta)$ is the density in the β phase. These scales introduce the dimensionless parameters

$$\mathscr{G}=\frac{G_\beta d}{T_M}, \tag{2.6}$$

$$\nu^*=\frac{\nu_\alpha}{\nu_\beta},\quad \kappa^*=\frac{\kappa_\alpha}{\kappa_\beta},\quad D^*=\frac{D_\alpha}{D_\beta},\quad \rho^*=\frac{\bar{\rho}_\alpha}{\bar{\rho}_\beta}, \tag{2.7}$$

$$\eta^*=\frac{\eta_\alpha}{\eta_\beta},\quad k^*=\frac{k_\alpha}{k_\beta},\quad G^*=\frac{G_\alpha}{G_\beta},\quad \mu^*=\frac{\mu_\alpha}{\mu_\beta}, \tag{2.8}$$

$$Pr=\frac{\nu_\beta}{\kappa_\beta},\quad Sc=\frac{\nu_\beta}{D_\beta},\quad Cr=\frac{\mu_\beta\kappa_\beta}{d\gamma},\quad Bo=\frac{g\rho_\beta d^2}{\gamma}, \tag{2.9}$$

$$\mathscr{G}Ra=\frac{g\eta_\beta G_\beta d^4}{\nu_\beta\kappa_\beta},\quad \mathscr{G}Ma=-\frac{\gamma_T G_\beta d^2}{\mu_\beta\kappa_\beta}, \tag{2.10}$$

$$\mathscr{L}_{\alpha\beta}/\mathscr{G}=\frac{\rho_\beta L_{\alpha\beta}\kappa_\beta}{k_\beta G_\beta d},\quad \tilde{m}_\alpha=\frac{m_\alpha}{T_M},\quad \tilde{m}_\beta=\frac{m_\beta}{T_M}, \tag{2.11}$$

and the geometrical parameter $H_\alpha=\bar{H}_\alpha/d$ representing the dimensionless depth of the α phase; the corresponding depth of the β phase is $H_\beta=1-H_\alpha$. Here $\mathscr{G}$ is the dimensionless temperature gradient in the β phase, ν^* is the ratio of kinematic viscosities, κ^* is the ratio of thermal diffusivities, D^* is the ratio of solute diffusivities, ρ^* is the ratio of densities, η^* is the ratio of thermal expansion coefficients, k^* is the ratio of thermal conductivities, G^* is the ratio of temperature gradients in the base state, μ^* is the ratio of dynamic viscosities, γ is the surface energy at $T=T_M$, γ_T is

Density ratio	$\rho^* = \rho^\alpha/\rho^\beta$	0.427
Kinematic viscosity ratio	$\nu^* = \nu^\alpha/\nu^\beta$	3.818
Dynamic viscosity ratio	$\mu^* = \mu^\alpha/\mu^\beta$	1.630
Thermal diffusivity ratio	$\kappa^* = \kappa^\alpha/\kappa^\beta$	1.137
Thermal conductivity ratio	$k^* = k^\alpha/k^\beta$	1.664
Thermal expansion ratio	$\eta^* = \eta^\alpha/\eta^\beta$	1.127
Diffusivity ratio	$D^* = D^\alpha/D^\beta$	1.0
Schmidt number	$Sc = \nu^\beta/D^\beta$	13.2
Prandtl number	$Pr = \nu^\beta/\kappa^\beta$	3.99×10^{-3}
Bond number	$Bo = g\rho^\beta d^2/\gamma$	233.1
Crispation number	$Cr = \mu^\beta\kappa^\beta/d\gamma$	8.420×10^{-5}
Marangoni number	$Ma = -\gamma_T T_E d/\mu_\beta\kappa_\beta$	92750.0
Rayleigh number	$Ra = g\eta_\beta T_E d^3/\nu_\beta\kappa_\beta$	259200.0
Dimensionless latent heat	$\mathscr{L}_{\alpha\beta} = \rho_\beta L_{\alpha\beta}\kappa_\beta/k_\beta T_E$	1.287
Dimensionless $\mathrm{d}T/\mathrm{d}c^\alpha$	$\tilde{m}_\alpha$	1.218
Dimensionless $-\mathrm{d}T/\mathrm{d}c^\beta$	$\tilde{m}_\beta$	5.152
Dimensionless $-\mathrm{d}T/\mathrm{d}p$	$\tilde{n}_{\alpha\alpha} = \tilde{n}_{\alpha\beta}$	1.865×10^{-13}
Dimensionless $-\mathrm{d}T/\mathrm{d}p$	$\tilde{n}_{\beta\alpha} = \tilde{n}_{\beta\beta}$	-1.949×10^{-13}

TABLE 3. Dimensionless properties of the aluminum–indium system at the monotectic temperature $T_M = 909.65$ K (636.5° C).

the derivative of γ with respect to temperature at $T = T_M$, Pr is the Prandtl number, Sc is the Schmidt number, Cr is the crispation number, Bo is the Bond number, g is the gravitational acceleration, $\mathscr{G}Ra$ is the Rayleigh number, $\mathscr{G}Ma$ is the Marangoni number, $\mathscr{L}_{\alpha\beta}/\mathscr{G}$ is the dimensionless latent heat and $\tilde{m}_\alpha$ and $\tilde{m}_\beta$ are dimensionless slopes of the coexistence curve. We consider the temperature gradient G_β to play the role of an experimental control parameter, and so have chosen to isolate the dependence on G_β in the dimensionless parameters in the single variable $\mathscr{G}$. The parameters Ra, Ma and $\mathscr{L}_{\alpha\beta}$ are then independent of the temperature gradient, and depend only on the geometry and material parameters. We note that $\mu^* = \rho^*\nu^*$ and $k^*G^* = 1$. Values of the dimensionless parameters for the aluminum–indium system are given in table 3.

2.5. *Linearized governing equations*

We assume a horizontal wavenumber a and a temporal growth rate $\sigma = \sigma_r + \mathrm{i}\sigma_i$; the perturbed interface $z = h(x, t)$ then has the specific form

$$z = \tilde{h}\exp(\mathrm{i}ax)\exp(\sigma_r t + \mathrm{i}\sigma_i t), \tag{2.12}$$

where $\tilde{h}$ is the dimensionless interface amplitude. Neutral stability corresponds to $\sigma_r = 0$. A direct mode of instability has $\sigma_i = 0$ ('exchange of stabilities'), whereas the case $\sigma_i \neq 0$ represents an oscillatory mode ('overstability'); for this problem oscillatory modes come in complex conjugate pairs.

The perturbed quantities (indicated by tildes) satisfy

$$\mathrm{i}a\tilde{u}^\alpha + \tilde{w}^\alpha_z = 0, \tag{2.13}$$

$$Pr^{-1}\sigma\,\tilde{u}^\alpha + ia\tilde{p}^\alpha/\rho^* = \nu^*(\tilde{u}^\alpha_{zz} - a^2\tilde{u}^\alpha), \tag{2.14}$$

$$Pr^{-1}\sigma\,\tilde{w}^\alpha + \tilde{p}^\alpha_z/\rho^* = \nu^*(\tilde{w}^\alpha_{zz} - a^2\tilde{w}^\alpha) + \eta^*\mathscr{G}Ra\tilde{T}^\alpha, \tag{2.15}$$

$$\sigma\,\tilde{T}^\alpha + G^*\tilde{w}^\alpha = \kappa^*(\tilde{T}^\alpha_{zz} - a^2\tilde{T}^\alpha), \tag{2.16}$$

$$Pr^{-1}\,Sc\,\sigma\,\tilde{c}^{\alpha} = D^{*}(\tilde{c}^{\alpha}_{zz} - a^{2}\tilde{c}^{\alpha}), \tag{2.17}$$

for $z > 0$, and

$$\mathrm{i}a\tilde{u}^{\beta} + \tilde{w}^{\beta}_{z} = 0, \tag{2.18}$$

$$Pr^{-1}\,\sigma\,\tilde{u}^{\beta} + \mathrm{i}a\,\tilde{p}^{\beta} = \tilde{u}^{\beta}_{zz} - a^{2}\tilde{u}^{\beta}, \tag{2.19}$$

$$Pr^{-1}\,\sigma\,\tilde{w}^{\beta} + \tilde{p}^{\beta}_{z} = \tilde{w}^{\beta}_{zz} - a^{2}\tilde{w}^{\beta} + \mathscr{G}Ra\tilde{T}^{\beta}, \tag{2.20}$$

$$\sigma\,\tilde{T}^{\beta} + \tilde{w}^{\beta} = \tilde{T}^{\beta}_{zz} - a^{2}\tilde{T}^{\beta}, \tag{2.21}$$

$$Pr^{-1}\,Sc\,\sigma\,\tilde{c}^{\beta} = (\tilde{c}^{\beta}_{zz} - a^{2}\tilde{c}^{\beta}), \tag{2.22}$$

for $z < 0$. Here $\tilde{w}^{\alpha}_{z}$ denotes the partial derivative $\partial\tilde{w}^{\alpha}/\partial z$, etc.

The boundary conditions at $z = 0$ are

$$\tilde{T}^{\alpha} + G^{*}\tilde{h} = \tilde{T}^{\beta} + \tilde{h}, \tag{2.23}$$

$$\tilde{u}^{\alpha} - \tilde{u}^{\beta} = 0, \tag{2.24}$$

$$(\tilde{p}^{\alpha} - \tilde{p}^{\beta}) - BoCr^{-1}(\rho^{*} - 1)\tilde{h} + a^{2}Cr^{-1}\tilde{h} = 2(\mu^{*}\tilde{w}^{\alpha}_{z} - \tilde{w}^{\beta}_{z}), \tag{2.25}$$

$$\left(\mu^{*}\tilde{u}^{\alpha}_{z} - \tilde{u}^{\beta}_{z}\right) + \mathrm{i}a\left(\mu^{*}\tilde{w}^{\alpha} - \tilde{w}^{\beta}\right) - \mathrm{i}a\,\mathscr{G}Ma\left(\tilde{T}^{\alpha} + G^{*}\tilde{h}\right) = 0, \tag{2.26}$$

$$\mathscr{G}\left[\tilde{T}^{\alpha} + G^{*}\tilde{h}\right] = \tilde{m}_{\alpha}\tilde{c}^{\alpha}, \tag{2.27}$$

$$\mathscr{G}\left[\tilde{T}^{\alpha} + G^{*}\tilde{h}\right] = -\tilde{m}_{\beta}\tilde{c}^{\beta}, \tag{2.28}$$

$$\rho^{*}(\tilde{w}^{\alpha} - \sigma\tilde{h}) = (\tilde{w}^{\beta} - \sigma\tilde{h}), \tag{2.29}$$

$$\mathscr{G}(k^{*}\tilde{T}^{\alpha}_{z} - \tilde{T}^{\beta}_{z}) = \rho^{*}(\tilde{w}^{\alpha} - \sigma\tilde{h})\mathscr{L}_{\alpha\beta}, \tag{2.30}$$

$$D^{*}\tilde{c}^{\alpha}_{z} - \tilde{c}^{\beta}_{z} = Pr^{-1}\,Sc\,\rho^{*}(\tilde{w}^{\alpha} - \sigma\tilde{h})\{\bar{c}^{\alpha} - \bar{c}^{\beta}\}. \tag{2.31}$$

The linearized differential equations have constant coefficients, and can be solved explicitly to obtain a determinant condition whose roots determine the growth rate σ as was done by Huang & Joseph (1992) for the single component problem. The system is large enough that the determinant equation cannot be solved analytically, and a numerical solution is required. In this work the determinant condition was solved symbolically for direct instabilities ($\sigma_r = 0$), and expanded for small wavenumbers to provide analytical insight concerning the dependence of $\mathscr{G}$ on layer depth and the other dimensionless parameters. We also computed the entire solution numerically using two additional methods: a matrix collocation procedure and a shooting procedure, as described previously (McFadden *et al.* 2007*a*,*b*). The matrix collocation procedure is based on a pseudospectral Chebyshev discretization of the solution, and provides an approximate set of growth rates for a given wavenumber and value of $\mathscr{G}$. In the shooting procedure a single growth rate is obtained by using the two-point boundary value solver BVSUP (Scott & Watts 1977), coupled with the root finder SNSQ (Powell 1970), both from the SLATEC library (Vandevender & Kaskell 1970), to implement a method described by Keller (1976) to solve the eigenvalue problem. The shooting procedure is generally more accurate but requires a good initial guess, which can be provided from the small wavenumber approximation, the collocation procedure, or previous solutions via continuation. The various solution procedures have been used to cross-validate the numerical results.

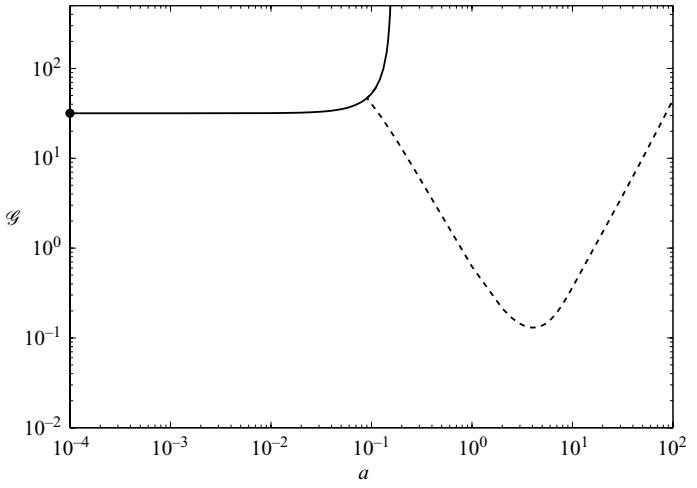

FIGURE 2. Neutral stability curves of thermocapillary modes ($Ma = 92\,750$) of the aluminum–indium system with equal layer depths for the case of heating from above ($\mathscr{G} > 0$) with buoyancy suppressed ($Ra = 0$). The resulting Marangoni instability has two branches, a direct mode with $\sigma_i = 0$ (solid curve) at low wavenumbers, and an oscillatory mode with $\sigma_i \neq 0$ (dashed curve) at larger wavenumbers. The dot indicates the corresponding analytical result from a small wavenumber approximation which agrees well with the numerical results.

3. Numerical results

For the given material properties of the aluminum–indium system, the stability results are functions of the wavenumber a, the dimensionless temperature gradient $\mathscr{G}$ and the dimensionless layer depth H_α. For a given layer depth, we plot neutral stability curves indicating values of $\mathscr{G}$ as a function of a for which $\sigma_r = 0$; the region of stability ($\sigma_r < 0$) generally lies in the direction of smaller values of $|\mathscr{G}|$. In this section we present numerical results for the case of equal layer depths ($H_\alpha = 1/2$). The results include neutral modes that persist to small wavenumbers, which we are able to describe by approximate analytical expressions in the next section. As these expression indicate that the small wavenumber behaviour is quite sensitive to the layer depths, we also include results for unequal layer depths to illustrate this behaviour. In order to help identify the mechanisms driving the instabilities we also compare results using the parameters in table 3 with idealized systems for which $Ra = 0$ or $Ma = 0$.

3.1. *Heating from above*

The case of heating from above corresponds to $G_\beta > 0$, so that $\mathscr{G}$ is positive. Neutral stability curves ($\sigma_r = 0$) for the case of Marangoni convection alone with buoyancy suppressed ($Ra = 0$, with relevance to low gravity conditions) are shown in figure 2. The most dangerous mode is oscillatory, with a critical wavenumber $a = 4.05$ and critical frequency $\sigma_i = \pm 1.0373$ for $\mathscr{G} = 0.1302$. For smaller wavenumbers the frequency decreases until it vanishes for $a = 0.11$ where the oscillatory mode merges with a direct mode of instability. The direct mode persists to small wavenumbers, and its asymptotic value of $\mathscr{G}$ can be predicted from a small wavenumber approximation for $Ra = 0$ given by

$$\mathscr{G} = -1.8535 \frac{(\rho^* - 1)Bo}{MaCr} = 31.7007 \tag{3.1}$$

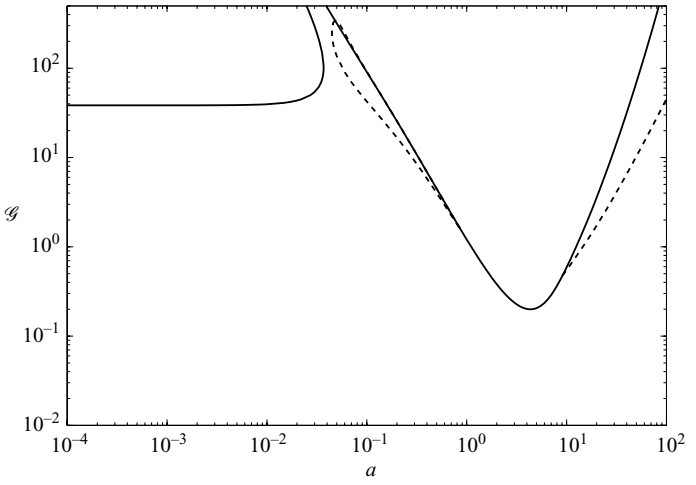

FIGURE 3. Neutral stability curves for equal layer depths for the case of heating from above ($\mathscr{G} > 0$) including both thermocapillarity ($Ma = 92\,750$) and buoyancy ($Ra = 259\,200$). Direct modes ($\sigma_i = 0$) are shown as solid curves, and oscillatory modes ($\sigma_i \neq 0$) are shown as dashed curves. A portion of the oscillatory mode corresponding to smaller wavenumbers is nearly coincident with the direct mode; this oscillatory mode actually forms a closed loop.

for the case of equal depths (the small wavenumber approximation is described in the next section). This result agrees with the numerical value for $a = 1.0 \times 10^{-4}$ to better than 4 digits. The direct mode exhibits pole-like behaviour near $a = 0.15$; for wavenumbers $a > 0.15$ the direct mode reappears with negative values of $\mathscr{G}$ (cf. figure 5 below).

In figure 3 we show the effects of including buoyancy ($Ra = 259\,200$ under terrestrial gravity), which for $\mathscr{G} > 0$ should be a stabilizing influence. The Boussinesq approximation should be valid for values of $|\mathscr{G}| \ll 10$, which ensures that the density variation with temperature is small (we show results for higher values only in order to indicate trends of the various effects). The most dangerous instability is now a direct mode, with a critical wavenumber $a = 4.35$ for $\mathscr{G} = 0.1996$. For smaller wavenumbers there is a closed oscillatory loop in close proximity to the small wavenumber side of the direct mode, and also there is a branch of an oscillatory mode for larger values of wavenumber; these oscillatory modes presumably result from the breakup of the most dangerous oscillatory mode with $Ra = 0$ in figure 2 under the stabilizing effects of buoyancy. Buoyancy effects have also stabilized the small wavenumber direct mode as well, which occurs for $\mathscr{G} = 38.45$.

3.2. *Heating from below*

The case of heating from below corresponds to $G_\beta < 0$, so that $\mathscr{G}$ is negative. The system is then potentially subject to buoyant modes of instability. With equal layer depths we find an oscillatory mode of instability at low wavenumbers, even in the absence of thermocapillarity and buoyancy ($Ra = Ma = 0$). Parameter studies indicate that critical values of $\mathscr{G}$ are found to be sensitive to the shape of the coexistence curve, the density and viscosity ratios and the layer depths, suggesting that the mode is a convectively-influenced phase-change mode; this is also evident from the small wavenumber expansions given below. A plot of the marginal values of $\mathscr{G}$ for this mode using the parameters in table 3 is shown in figure 4.

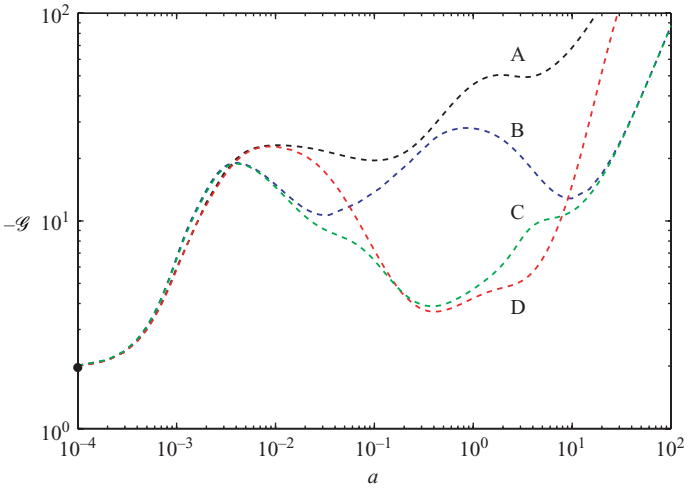

FIGURE 4. Neutral stability curves ($\sigma_i \neq 0$) for equal layer depths heated from below ($\mathscr{G} < 0$) for the phase-change mode. For curve A: $Ma = Ra = 0$; for curve B: $Ma = 92\,750$ and $Ra = 0$; for curve C: $Ma = 92\,750$ and $Ra = 259\,200$; and for curve D: $Ma = 0$ and $Ra = 259\,200$. The dot indicates the corresponding analytical result from a small wavenumber approximation which agrees well with the numerical results.

The phase-change mode persists in the presence of both thermocapillarity and buoyancy, although the marginal values are affected as also indicated in figure 4. The critical wavenumber corresponds to $a = 0$, and the small wavenumber approximation for $Ra = Ma = 0$ and equal depths gives the result

$$\mathscr{G} = -0.5838 \frac{\tilde{m}_\alpha \tilde{m}_\beta \{\bar{c}^\alpha - \bar{c}^\beta\}(1 + k^*)}{[\tilde{m}_\alpha - \tilde{m}_\beta]} = -1.9670, \tag{3.2}$$

and

$$\sigma_i^2 = 0.02846\, a^2\, Pr\, D^* \left(\frac{Bo}{Cr}\right) \frac{[\tilde{m}_\alpha - \tilde{m}_\beta]}{\{Sc\,[\tilde{m}_\alpha\, D^* - \tilde{m}_\beta]\}} = 23.8146\, a^2, \tag{3.3}$$

which yields $\sigma_i = \pm 4.880 \times 10^{-4}$ for $a = 1.0 \times 10^{-4}$. These results are in good agreement with the numerical results, $\mathscr{G} = -2.009$ and $\sigma_i = \pm 4.886 \times 10^{-4}$, for $a = 1.0 \times 10^{-4}$.

Neutral stability curves for the case of Marangoni convection alone with buoyancy suppressed ($Ra = 0$) are shown in figure 5. Although the oscillatory phase change mode persists, the most dangerous instability is a direct Marangoni mode with a critical wavenumber $a = 4.00$ for $\mathscr{G} = -0.2002$. As noted above, this direct mode exhibits pole-like behaviour near $a = 0.15$ (cf. figure 2), and is increasingly stable at large wavenumbers.

If the destabilizing effects of buoyancy are included, there are many additional thermal modes of instability in the two layers. For example, if the true interface is replaced by an idealized interface that is isothermal, non-deformable and impermeable to solute, there are two decoupled families of buoyant modes featuring stacked convective cells in each layer with no interaction between the layers. For the actual phase-change boundary with heat and mass transport through the interface these modes are weakly coupled, as shown in figure 6 with the effects of thermocapillarity ignored. More specifically, where the curves for the uncoupled modes cross, the weakly coupled modes have near-intersections in which the crossing points are replaced by

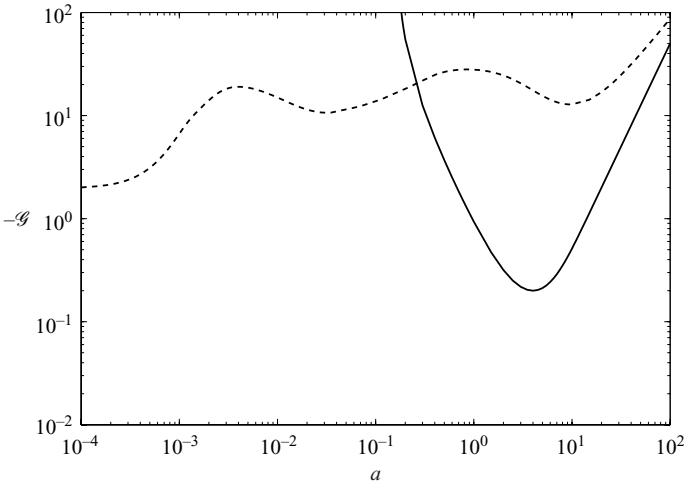

FIGURE 5. Neutral stability curves for equal layer depths heated from below ($\mathscr{G} < 0$) including the effects of thermocapillarity ($Ma = 92\,750$) but with buoyancy suppressed ($Ra = 0$). The oscillatory phase change mode (dashed curve) extends to small wavenumbers, and the direct Marangoni mode (solid curve) is the most dangerous instability.

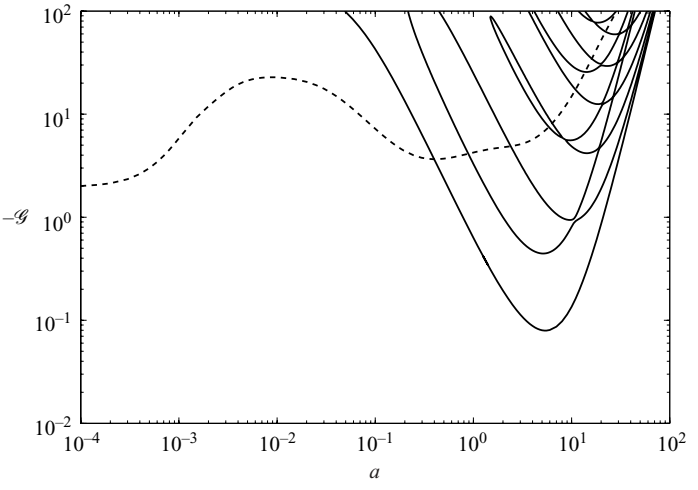

FIGURE 6. Neutral stability curves for equal layer depths heated from below ($\mathscr{G} < 0$) including the effects of buoyancy ($Ra = 259\,200$) but with thermocapillarity suppressed ($Ma = 0$). The oscillatory phase change mode (dashed curve) extends to small wavenumbers, and a family of direct thermal buoyancy modes (solid curves) includes the most dangerous instability.

smooth transitions where the modes exchange identity; these interactions occur over narrow regions of parameter space which are not well resolved in figure 6. The most dangerous mode is a direct mode for $a = 5.40$ with $\mathscr{G} = -0.07938$. There is a single circulation cell in the lower layer (β phase), with a single, weaker, counter-rotating cell in the upper layer. In contrast, the next higher direct thermal mode with $\mathscr{G} = -0.4448$, has a single circulation cell in the upper layer (α phase), with a single, weaker, counter-rotating cell in the lower layer. Many more modes featuring

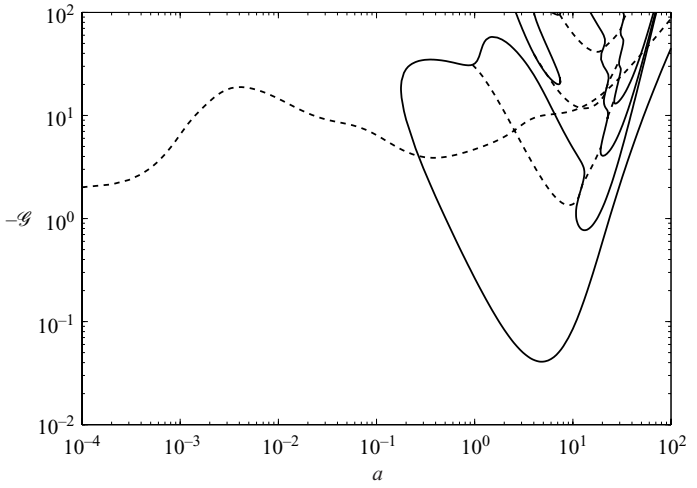

FIGURE 7. Neutral stability curves for equal layer depths heated from below ($\mathscr{G} < 0$) including the effects of both buoyancy ($Ra = 259\,200$) and thermocapillarity ($Ma = 92\,750$). The oscillatory phase change mode extends to small wavenumbers, and additional oscillatory instabilities occur athwart the direct modes under the combined effects of buoyancy and thermocapillarity.

increasing numbers of stacked convection cells occur for increasing values of $|\mathscr{G}|$; the first few are shown in figure 6. The oscillatory phase change mode is also present.

Neutral curves showing the effects of both buoyancy and thermocapillarity are shown in figure 7. The most dangerous instability is a direct mode for $a = 4.80$ with $\mathscr{G} = -0.04081$; the addition of thermocapillarity has slightly destabilized the system. For higher values of $|\mathscr{G}|$ the interactions are much more complicated, including oscillatory modes that occur where coupled direct modes appear to cross.

4. Small wavenumber approximations

Linear instabilities that persist to small wavenumbers occur for both the Marangoni mode and the phase-change mode. Approximate conditions for instability may be obtained analytically for these two cases, which we outline in this section. For simplicity we ignore the effect of buoyancy, which does not play a significant role in the small wavenumber instabilities.

4.1. *Marangoni mode*

For small wavenumbers with $Ra = 0$ the direct mode representing a thermocapillary instability (cf. figure 2) can be computed analytically. The equations have an approximate solution with linear temperature fields, and constant pressure and solute fields. Specifically, we find

$$\tilde{T}^{\alpha}(z) = \frac{(G^* - 1)}{(H_\alpha + k^* H_\beta)}(z - H_\alpha)\tilde{h}, \quad \tilde{T}^{\beta}(z) = \frac{k^*(G^* - 1)}{(H_\alpha + k^* H_\beta)}(z + H_\beta)\tilde{h}, \tag{4.1}$$

$$\tilde{c}^{\alpha}(z) = \frac{\mathscr{G}}{\tilde{m}_\alpha(H_\alpha + k^* H_\beta)}\tilde{h}, \quad \tilde{c}^{\beta}(z) = \frac{-\mathscr{G}}{\tilde{m}_\beta(H_\alpha + k^* H_\beta)}\tilde{h}, \tag{4.2}$$

$$\tilde{p}^{\alpha}(z) = P^{\alpha} = -\frac{\mu^* H_\beta^2 Bo(\rho^* - 1)}{Cr[H_\alpha^2 - \mu^* H_\beta^2]}\tilde{h}, \quad \tilde{p}^{\beta}(z) = P^{\beta} = -\frac{H_\alpha^2 Bo(\rho^* - 1)}{Cr[H_\alpha^2 - \mu^* H_\beta^2]}\tilde{h}, \tag{4.3}$$

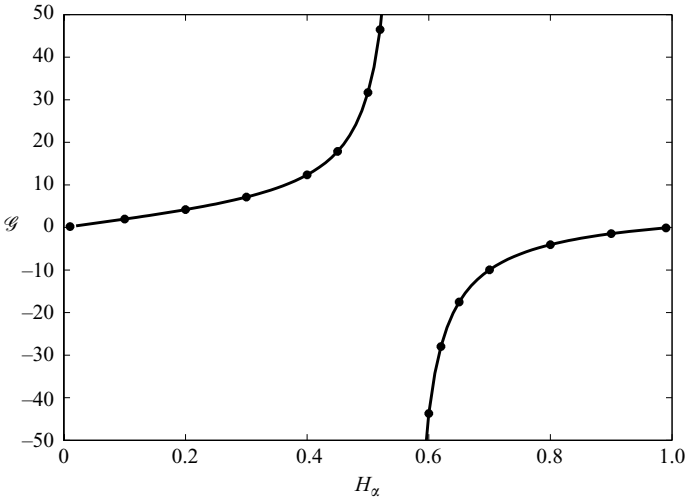

FIGURE 8. Neutral stability results (solid curve) for the small wavenumber approximation to the direct thermocapillary mode ($Ma = 92\,750$) as a function of the dimensionless layer depth H_α, excluding the effects of buoyancy ($Ra = 0$). The data points are results from the full numerical calculation with $a = 1.0 \times 10^{-4}$. For values of $H_\alpha < \sqrt{\mu^*}/(1 + \sqrt{\mu^*}) \approx 0.56$ the instability occurs for heating from above ($\mathscr{G} > 0$), and for $H_\alpha > 0.56$ the instability occurs for heating from below ($\mathscr{G} < 0$). The stable region ($\sigma_r < 0$) lies between the two curves, and includes the region where $|\mathscr{G}|$ is small.

$$\tilde{u}^\alpha(z) = \frac{\mathrm{i}aP^\alpha}{2\mu^*}(z - H_\alpha)^2 + \frac{\mathrm{i}aP^\alpha}{3\mu^*}H_\alpha(z - H_\alpha), \quad \tilde{u}^\beta(z) = \frac{\mathrm{i}aP^\beta}{2}(z + H_\beta)^2 - \frac{\mathrm{i}aP^\beta}{3}H_\beta(z + H_\beta), \tag{4.4}$$

$$\tilde{w}^\alpha(z) = \frac{a^2P^\alpha}{6\mu^*}z(z - H_\alpha)^2, \quad \tilde{w}^\beta(z) = \frac{a^2P^\beta}{6}z(z + H_\beta)^2. \tag{4.5}$$

The corresponding critical temperature gradient is

$$\mathscr{G} = \frac{2H_\alpha H_\beta[H_\alpha + \mu^* H_\beta][H_\alpha + k^* H_\beta]}{3[H_\alpha^2 - \mu^* H_\beta^2]}\frac{(\rho^* - 1)Bo}{MaCr}. \tag{4.6}$$

Note that $\mathscr{G}$ has a pole where $H_\alpha^2 = \mu^* H_\beta^2$, so that the sign of $\mathscr{G}$ depends on the layer depth. For the aluminum–indium system with a viscosity ratio $\mu^* = 1.630$, the pole occurs for $H_\alpha = \sqrt{\mu^*}/(1 + \sqrt{\mu^*}) = 0.56$ (see figure 8).

4.2. *Phase-change mode*

For small wavenumbers the numerical results indicate that the phase-change mode is an oscillatory instability (see figure 4) with a frequency that tends to zero for small wavenumbers (see (4.24)). An approximate analysis may be performed in which the frequency is only retained in the solute diffusion equations, and the interfacial mass and solute flux balance boundary conditions. The equations have an approximate solution with linear temperature fields, and constant pressure fields. Specifically, we find

$$\tilde{T}^\alpha(z) = A^\alpha(z - H_\alpha), \quad \tilde{T}^\beta(z) = A^\beta(z + H_\beta), \tag{4.7}$$

$$\tilde{p}^\alpha(z) = P^\alpha, \quad \tilde{p}^\beta(z) = P^\beta, \tag{4.8}$$

$$\tilde{u}^\alpha(z) = \frac{\mathrm{i}aP^\alpha}{2\mu^*}(z - H_\alpha)^2 + E^\alpha(z - H_\alpha), \quad \tilde{u}^\beta(z) = \frac{\mathrm{i}aP^\beta}{2}(z + H_\beta)^2 + E^\beta(z + H_\beta), \tag{4.9}$$

$$\tilde{w}^{\alpha}(z) = \frac{a^2 P^{\alpha}}{6\mu^*}(z - H_{\alpha})^3 - \frac{\mathrm{i}aE^{\alpha}}{2}(z - H_{\alpha})^2, \quad \tilde{w}^{\beta}(z) = \frac{a^2 P^{\beta}}{6}(z + H_{\beta})^3 - \frac{\mathrm{i}aE^{\beta}}{2}(z + H_{\beta})^2, \tag{4.10}$$

$$\tilde{c}^{\alpha}(z) = F^{\alpha}\cosh\left(\sqrt{Sc\,\sigma/PrD^*}[z - H_{\alpha}]\right), \quad \tilde{c}^{\beta}(z) = F^{\beta}\cosh\left(\sqrt{Sc\,\sigma/Pr}[z + H_{\beta}]\right), \tag{4.11}$$

where

$$A^{\alpha} = \frac{(G^* - 1)}{(H_{\alpha} + k^* H_{\beta})}\tilde{h}, \quad A^{\beta} = \frac{k^*(G^* - 1)}{(H_{\alpha} + k^* H_{\beta})}\tilde{h}, \tag{4.12}$$

$$F^{\alpha} = \frac{\mathscr{G}}{\tilde{m}_{\alpha}(H_{\alpha} + k^* H_{\beta})}\frac{\tilde{h}}{\cosh\left(\sqrt{Sc\,\sigma/PrD^*}H_{\alpha}\right)}, \tag{4.13}$$

$$F^{\beta} = \frac{-\mathscr{G}}{\tilde{m}_{\beta}(H_{\alpha} + k^* H_{\beta})}\frac{\tilde{h}}{\cosh\left(\sqrt{Sc\,\sigma/Pr}H_{\beta}\right)}, \tag{4.14}$$

$$E^{\alpha} = \frac{\mathrm{i}aH_{\alpha}[H_{\alpha} + 2\mu^* H_{\beta}]P^{\alpha}}{2\mu^*[H_{\alpha} + \mu^* H_{\beta}]} + \frac{\mathrm{i}aH_{\beta}^2 P^{\beta}}{2[H_{\alpha} + \mu^* H_{\beta}]}, \tag{4.15}$$

$$E^{\beta} = \frac{-\mathrm{i}aH_{\alpha}^2 P^{\alpha}}{2[H_{\alpha} + \mu^* H_{\beta}]} - \frac{\mathrm{i}aH_{\beta}[2H_{\alpha} + \mu^* H_{\beta}]P^{\beta}}{2[H_{\alpha} + \mu^* H_{\beta}]}, \tag{4.16}$$

$$P^{\alpha} = \frac{(\rho^* - 1)[\sigma + a^2 a_2\, Bo/Cr]}{a^2(a_1 + a_2)}\tilde{h}, \quad P^{\beta} = \frac{(\rho^* - 1)[\sigma - a^2 a_1\, Bo/Cr]}{a^2(a_1 + a_2)}\tilde{h}. \tag{4.17}$$

Here

$$a_1 = \rho^*\frac{H_{\alpha}^3[H_{\alpha} + 4\mu^* H_{\beta}]}{12\mu^*[H_{\alpha} + \mu^* H_{\beta}]} + \frac{H_{\alpha}^2 H_{\beta}^2}{4[H_{\alpha} + \mu^* H_{\beta}]}, \quad a_2 = \rho^*\frac{H_{\alpha}^2 H_{\beta}^2}{4[H_{\alpha} + \mu^* H_{\beta}]} + \frac{H_{\beta}^3[4H_{\alpha} + \mu^* H_{\beta}]}{12[H_{\alpha} + \mu^* H_{\beta}]}. \tag{4.18}$$

The dispersion relation is then found to take the form

$$-\frac{D^*\mathscr{G}\sqrt{Sc\,\sigma/PrD^*}}{\tilde{m}_{\alpha}(H_{\alpha} + k^* H_{\beta})}\tanh\left(\sqrt{Sc\,\sigma/PrD^*}H_{\alpha}\right)\tilde{h} + \frac{\mathscr{G}\sqrt{Sc\,\sigma/Pr}}{\tilde{m}_{\beta}(H_{\alpha} + k^* H_{\beta})}\tanh\left(\sqrt{Sc\,\sigma/Pr}H_{\beta}\right)\tilde{h}$$

$$= Pr^{-1}\,Sc\,\rho^*\left(\tilde{w}^{\alpha} - \sigma\tilde{h}\right)\{\bar{c}^{\alpha} - \bar{c}^{\beta}\}, \tag{4.19}$$

where

$$\tilde{w}^{\alpha} = d_1\sigma\tilde{h} + d_2\frac{a^2\, Bo}{Cr}\tilde{h}, \tag{4.20}$$

with

$$d_1 = \frac{(\rho^* - 1)}{12\mu^*(a_1 + a_2)[H_{\alpha} + \mu^* H_{\beta}]}\left[H_{\alpha}^3[H_{\alpha} + 4\mu^* H_{\beta}] + 3\mu^* H_{\alpha}^2 H_{\beta}^2\right], \tag{4.21}$$

$$d_2 = \frac{(\rho^* - 1)}{12\mu^*(a_1 + a_2)[H_{\alpha} + \mu^* H_{\beta}]}\left[H_{\alpha}^3 a_2[H_{\alpha} + 4\mu^* H_{\beta}] - 3\mu^* a_1 H_{\alpha}^2 H_{\beta}^2\right]. \tag{4.22}$$

The dispersion relation is highly nonlinear and still requires a numerical solution to find the roots. For example, in figure 9 we show a comparison of the results using the numerical solution without approximation for $a = 1.0 \times 10^{-4}$ (symbols) and

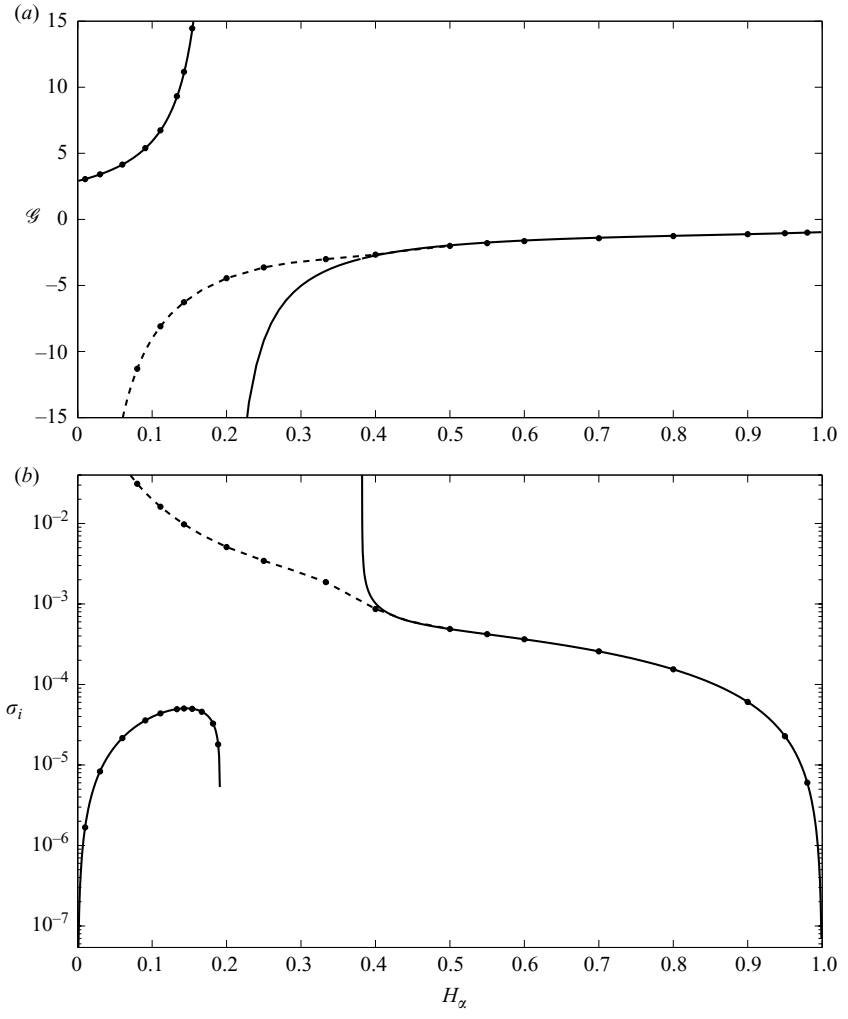

FIGURE 9. Neutral stability curves showing $\mathscr{G}$ (*a*) and σ_i (*b*) with $a = 1.0 \times 10^{-4}$ for the oscillatory phase-change mode as a function of the dimensionless layer depth H_α, excluding the effects of thermocapillarity ($Ma = 0$) and buoyancy ($Ra = 0$). The symbols indicate results obtained using the full numerical scheme without approximation. The dashed curve indicated results obtained using the small wavenumber approximation (4.19). The solid curves indicate results using the simplified relations in (4.23) and (4.24). In the upper plot the stable region ($\sigma_r < 0$) lies between the solid curves, and includes the region where $|\mathscr{G}|$ is small.

the roots of the above small wavenumber approximation (dashed curve). The small wavenumber approximation is in good agreement with the full numerical results. For small depths $H_\alpha < 0.15$ there are two roots for $\mathscr{G}$ having opposite signs, indicating instability for heating from both above and below. The solution branch with $\mathscr{G} > 0$ is increasingly stabilized as H_α approaches $H_\alpha = 0.15$, and the corresponding frequencies σ_i tend to zero. The solution branch with $\mathscr{G} < 0$ has large negative values of $\mathscr{G}$ for small depths H_α, and the frequency σ_i also becomes large. This branch persists for $H_\alpha > 0.15$; both the frequencies and the magnitude of $\mathscr{G}$ decrease for increasing H_α.

A further simplification to the small wavenumber dispersion relation in (4.19) can be found by expanding the hyperbolic tangent functions by writing $\tanh y \approx y - y^3/3$,

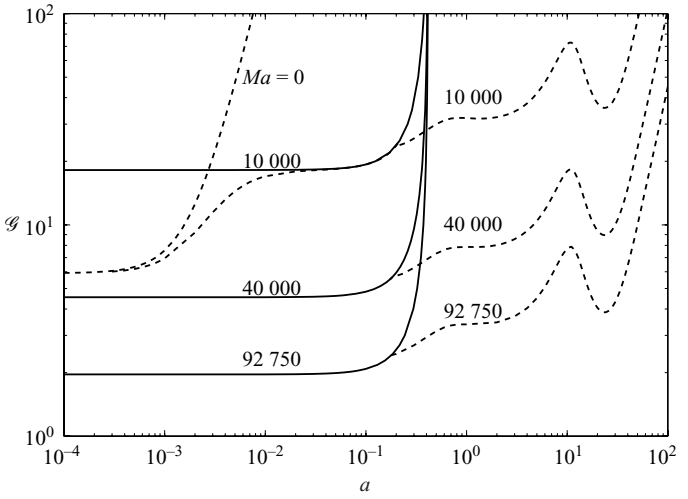

FIGURE 10. Neutral stability curves for the oscillatory phase-change mode (dashed curves) and the direct Marangoni mode (solid curves) for the case of heating from above $\mathscr{G} > 0$ with $H_\alpha = 0.1$, excluding the effects of buoyancy ($Ra = 0$), for various values of Ma.

which is a good approximation for small frequencies. The real and imaginary parts of the resulting expression then give the more useful approximate relations

$$\mathscr{G}\left[\frac{H_\beta}{\tilde{m}_\beta} - \frac{H_\alpha}{\tilde{m}_\alpha}\right] = \rho^*(d_1 - 1)\{\bar{c}^\alpha - \bar{c}^\beta\}(H_\alpha + k^* H_\beta), \tag{4.23}$$

$$\sigma_i^2 = 3\,Pr\,D^*\left(d_2\frac{a^2\,Bo}{Cr}\right)\left[\tilde{m}_\alpha H_\beta - \tilde{m}_\beta H_\alpha\right] / \left\{Sc(d_1 - 1)\left[\tilde{m}_\alpha\,D^*\,H_\beta^3 - \tilde{m}_\beta H_\alpha^3\right]\right\}. \tag{4.24}$$

Results using this approximation are also shown in figure 9 (solid curves). For our system this approximation works well for the mode with $\mathscr{G} < 0$ for $H_\alpha > 0.40$, and also works well for the mode with $\mathscr{G} > 0$ for $H_\alpha < 0.2$. For intermediate values in the range $0.2 < H_\alpha < 0.4$, (4.24) predicts negative values for σ_i^2; specifically, (4.24) produces $\sigma_i = 0$ for $H_\alpha = \tilde{m}_\alpha/(\tilde{m}_\alpha + \tilde{m}_\beta) \approx 0.2$; at this depth (4.23) exhibits a pole for $\mathscr{G}$. Equation (4.24) produces a pole in σ_i for $H_\alpha = (D^*\tilde{m}_\alpha)^{1/3}/((D^*\tilde{m}_\alpha)^{1/3} + \tilde{m}_\beta^{1/3}) \approx 0.4$. This range of depths over which the simplified approximation breaks down corresponds to the interval where the full numerical solution for σ_i is no longer small, in our case with $|\sigma_i| \geqslant 10^{-3}$.

In figure 10 we show numerical results for a depth $H_\alpha = 0.1$ and $Ra = 0$. In contrast to the previous results for $H_\alpha = 0.5$, these conditions allow the phase-change mode to occur if the layers are heated from above with $\mathscr{G} > 0$. For $Ma = 0$, the most dangerous wavenumber is $a = 0$, and the mode is stabilized for increasing wavenumbers. The behaviour of the phase-change mode becomes complicated as the effects of thermocapillarity become important. For $Ma = 10\,000$ a direct Marangoni mode lies above the oscillatory phase-change mode. The two modes have similar values of $\mathscr{G}$ over a range of wavenumbers, after which the Marangoni mode is stabilized near $a = 0.4$; the oscillatory mode persists to larger wavenumbers. For $Ma = 40\,000$ the Marangoni mode is most dangerous for $a = 0$, and the oscillatory mode branches off the direct mode at a finite wavenumber and does not persist to

small wavenumbers. This trend continues for $Ma = 92\,750$, as the Marangoni mode is increasingly unstable.

5. Discussion

The phase-change mode we have described for the two-component aluminum–indium system is reminiscent of the oscillatory mode computed by Huang & Joseph (1992) for the single-component water-steam system. The single-component mode is a convective instability driven by the coupling between interfacial temperature and pressure as discussed in McFadden & Coriell (2009). The oscillatory phase-change mode in the aluminum–indium system is also a convective instability, but is driven by solute diffusion, as can be seen from the approximate expressions in (4.23) and (4.24) derived in the small wavenumber limit. This mode is predicted to occur for heating from below for thin layers of the β-phase, and can occur for either heating from above or below in the other extreme. A constitutional supercooling argument (Tiller *et al.* 1953; Coriell & McFadden 1994) would suggest that instabilities might be expected in either case, although if either layer becomes relatively thin the strong influence of nearby isothermal no-slip boundaries on suppressing flow and temperature fluctuations would be expected to provide a stabilizing effect in that layer. We have assumed both liquid phases are in contact only at the phase boundary $z = h(x, t)$; the possibility of bulk nucleation of one phase in the interior of the other, and/or spinodal decomposition, is neglected.

The pressure effects that are important in the single-component phase-change mode act through the Clausius–Clapeyron relation that relates the interfacial pressure and temperature. For the two-component case, the stronger coupling is between temperature and solute through the equilibrium relations in (2.27) and (2.28). A pressure effect does enter into a more complete version of this boundary condition, which is the linearized form of the thermodynamic equilibrium conditions $\tilde{\mu}_A(T^\alpha, p^\alpha, c^\alpha) = \tilde{\mu}_A(T^\beta, p^\beta, c^\beta)$ and $\tilde{\mu}_B(T^\alpha, p^\alpha, c^\alpha) = \tilde{\mu}_B(T^\beta, p^\beta, c^\beta)$, but for liquids that are well removed from the critical point the effects of pressure in these relations are negligible, as, for example,

$$\left| \frac{\partial \tilde{\mu}_A}{\partial p^\alpha} \tilde{p}^\alpha \right| \ll \left| \frac{\partial \tilde{\mu}_A}{\partial c^\alpha} \tilde{c}^\alpha \right|. \tag{5.1}$$

More specifically, the linearized versions of these dimensionless boundary conditions take the form

$$\mathscr{G}\left[\tilde{T}^\alpha + G^* \tilde{h}\right] = \tilde{m}_\alpha \tilde{c}^\alpha + \tilde{n}_{\alpha\alpha}\left[\tilde{p}^\alpha - \rho^* \frac{Bo}{Cr}\tilde{h}\right] - \tilde{n}_{\alpha\beta}\left[\tilde{p}^\beta - \frac{Bo}{Cr}\tilde{h}\right], \tag{5.2}$$

$$\mathscr{G}\left[\tilde{T}^\alpha + G^* \tilde{h}\right] = -\tilde{m}_\beta \tilde{c}^\beta + \tilde{n}_{\beta\alpha}\left[\tilde{p}^\alpha - \rho^* \frac{Bo}{Cr}\tilde{h}\right] - \tilde{n}_{\beta\beta}\left[\tilde{p}^\beta - \frac{Bo}{Cr}\tilde{h}\right], \tag{5.3}$$

where $\tilde{n}_{\alpha\alpha} = \tilde{n}_{\alpha\beta}$ and $\tilde{n}_{\beta\beta} = \tilde{n}_{\beta\alpha}$ are all of the order of 10^{-13} (see table 3); since numerical calculations indicate that these terms are unimportant, we have neglected these terms for simplicity in our model.

We have also neglected pressure effects in the surface energy, which we have taken to depend only on temperature. The Gibbs adsorption equation relates thermodynamic variations in surface energy to changes in the interfacial temperature and chemical potentials, and these variables are constrained to lie on the co-existence curve at a given pressure. Extremely large deviations from atmospheric pressure are required to

produce changes in these relations, and so for simplicity we have also neglected the effects of pressure variations on the surface energy.

The range of temperature variations allowed in the Boussinesq approximation provides further limitations on the accuracy of our model. The temperature difference across our system is given in dimensional terms by $\Delta T \approx \mathscr{G} T_M$, where $T_M = 909.65$ K. The critical values of $\mathscr{G}$ for buoyant modes that we calculate are of the order of 0.1 or less in magnitude, depending on the layer depth, corresponding to heating by roughly a hundred degrees Kelvin or less, which is not unreasonable in metallic systems. Smaller variations of temperature for instability of the phase-change mode would be required for conditions closer to the thermodynamic critical point of the system where the slopes $\tilde{m}_\alpha$ and $\tilde{m}_\beta$ are reduced.

6. Conclusion

We have performed linear stability calculations for horizontal fluid bilayers in a two-component system that can undergo a phase transformation, taking into account both buoyancy effects and thermocapillary effects. We have obtained values for the applied temperature difference across the system that is necessary to produce instability by a linear stability analysis, using numerical and small wavenumber approximations. In addition to buoyant and thermocapillary modes of instability, we find an oscillatory phase-change instability due to the combined effects of solute diffusion and fluid flow that persists at small wavenumbers. This mode is sensitive to the ratio of the layer depths, and for certain depths can occur for heating from either above or below. The combined effects of buoyancy and thermocapillarity during heat and mass transport provide a wealth of coupled instabilities in this simple system, illustrating the challenges that arise in materials processing applications for multicomponent systems.

It is a pleasure to acknowledge S. H. Davis, who has provided exemplary scientific inspiration and congeniality to generations of students and colleagues in fluid mechanics and applied mathematics. The authors are grateful for helpful discussions with Ursula Kattner, who provided the reference to the work by Coughanowr (1989).

Appendix

An assessment for the aluminum–indium system by Coughanowr (1989) produced an explicit model for the molar Gibbs free energy $\bar{g}_m(T, p, X) = X\bar{\mu}_{In}(T, p, X) + (1 - X)\bar{\mu}_{Al}(T, p, X)$. Here $\bar{\mu}_{Al}$ and $\bar{\mu}_{In}$ are the chemical potentials (per mole) of aluminum and indium, and T, p and X are the temperature, pressure and mole fraction of indium, respectively. Specifically, at atmospheric pressure p_R we have

$$\bar{\mu}_{Al}(T, p_R, X) = \bar{\mu}^0_{Al}(T) + R\,T\,\log(1 - X) + a_0 X^2 + a_1(3X^2 - 4X^3) + a_2(5X^2 - 16X^3 + 12X^4), \quad \text{(A 1)}$$

$$\bar{\mu}_{In}(T, p_R, X) = \bar{\mu}^0_{In}(T) + R\,T\,\log(X) + a_0(1 - X)^2 + a_1(1 - 6X + 9X^2 - 4X^3) + a_2(5X^2 - 16X^3 + 12X^4), \quad \text{(A 2)}$$

where $\bar{\mu}^0_{Al} = (10711.0 - 11.473\,T)$, $\bar{\mu}^0_{In} = (3283.0 - 7.639\,T)$, $a_0 = (21259.6 - 0.48737\,T)$, $a_1 = (3850.3 - 1.20564\,T)$, and $a_2 = (5479.2 - 3.16805\,T)$. Here the chemical potentials are in J mol^{-1}, T is in K and $R = 8.3143$ J (K·mol)$^{-1}$ is the ideal gas constant.

In this work we further assume

$$\bar{\mu}_{Al}(T, p, X) = \bar{\mu}_{Al}(T, p_R, X) + \bar{V}_{Al}(T)[p - p_R], \tag{A 3}$$

$$\bar{\mu}_{In}(T, p, X) = \bar{\mu}_{In}(T, p_R, X) + \bar{V}_{In}(T)[p - p_R], \tag{A 4}$$

where the partial molar volumes $\bar{V}_{Al}$ and $\bar{V}_{In}$ depend only on temperature. Their values may then be determined from the densities of pure aluminum and indium, and their molecular weights $\omega_{Al} = 0.0269815$ kg mol^{-1} and $\omega_{In} = 0.114818$ kg mol^{-1}. In the governing equations it is convenient to replace the mole fraction X by the corresponding mass fraction c; they are related by $c = X\omega_{In}/[X\omega_{In} + (1 - X)\omega_{Al}]$. In the resulting model the liquid density (in either phase) depends only on temperature and composition, and satisfies

$$\frac{1}{\rho(T, c)} = \frac{c}{\rho_{In}(T)} + \frac{(1 - c)}{\rho_{Al}(T)}, \tag{A 5}$$

Following Gale & Totemeier (2004) we take the densities of the pure components to be $\rho_{Al}(T) = 2385 - 0.2800(T - 933.15)$ kg m^{-3} and $\rho_{In}(T) = 7023 - 0.6798(T - 429.75)$ kg m^{-3}. The dynamic viscosities have the Arrhenius form

$$\mu = \mu_0 \exp(E_0/RT), \tag{A 6}$$

where μ_0 and E_0 are constants. For aluminum, $T_0 = 660.0$ C, $\mu_0 = 0.1492 \times 10^{-3}$ N s m^{-2} and $E_0 = 16.5 \times 10^3$ J mol^{-1}. For indium, $T_0 = 156.6$ C, $\mu_0 = 0.302 \times 10^{-3}$ N s m^{-2} and $E_0 = 6.65 \times 10^3$ J mol^{-1}.

The surface energy is given by

$$\gamma = \gamma_0 \left(1 - \frac{T}{T_0}\right)^{\delta}, \tag{A 7}$$

where $T_0 = 838$ C, $\gamma_0 = 508.0 \times 10^{-3}$ J m^{-2} and $\delta = 1.73$ (Merkwitz & Hoyer 1999). Then

$$\frac{\mathrm{d}\gamma}{\mathrm{d}T} = \frac{-\delta\,\gamma}{(T_0 - T)}. \tag{A 8}$$

REFERENCES

Andereck, C. D., Colovas, P. W., Degen, M. M. & Renardy, Y. Y. 1998 Instabilities in two-layer Rayleigh–Benard convection: overview and outlook. *Int. J. Engng Sci.* **36**, 1451–1470.

Berg, R. F. & Moldover, M. R. 1989 Critical exponent for the viscosity of four binary liquids. *J. Chem. Phys.* **89**, 3694–3704.

Bräuer, P. & Müller-Vogt, G. 1998 Measurements of aluminum diffusion in molten gallium and indium. *J. Cryst. Growth* **186**, 520–527.

Busse, F. H. 1989 Fundmanetals of thermal convection. In *Mantle Convection: Plate Tectonics and Global Dynamics* (ed. W. Peltier), pp. 23–95. Gordon & Breach.

Busse, F. & Schubert, G. 1971 Convection in a fluid with two phases. *J. Fluid Mech.* **46**, 801–812.

Coriell, S. R. & McFadden, G. B. 1994 Morphological stability. In *Handbook of Crystal Growth 1. Fundamentals, Part B: Transport and Stability* (ed. D. T. J. Hurle), pp. 785–857. North-Holland.

Coriell, S. R., Mitchell, W. F., Murray, B. T., Andrews, J. B. & Arikawa, Y. 1997 Analysis of monotectic growth: infinite diffusion in the L2-phase. *J. Cryst. Growth* **179**, 647–657.

Coughanowr, C. A. 1989 Solid-state electrochemistry and thermodynamic assessment in the Al-In-Sb system. PhD thesis, Department of Chemical Engineering, University of Florida, Gainesville, FL.

Davis, S. H. 1987 Thermocapillary instabilities. *Annu. Rev. Fluid Mech.* **19**, 403–435.

Davis, S. H. 1994 Effects of fluid flow on morphological stability. In *Handbook of Crystal Growth 1. Fundamentals, Part B: Transport and Stability* (ed. D. T. J. Hurle), pp. 859–897. North-Holland.

Davis, S. H. 2001 *Theory of Solidification*. Cambridge University Press.

Derby, B. & Favier, J. J. 1983 A criterion for the determination of monotectic structure. *Acta Metall.* **31** (7), 1123–1130.

Gale, W. F. & Totemeier, T. C. (Ed.) 2004 *Smithells' Metals Reference Book*. Elsevier Butterworth-Heinemann.

Glicksman, M. E., Coriell, S. R. & McFadden, G. B. 1986 Interaction of flows with the crystal-melt interface. *Annu. Rev. Fluid Mech.* **18**, 307–335.

Huang, A. & Joseph, D. D. 1992 Instability of the equilibrium of a liquid below its vapour between horizontal heated plates. *J. Fluid Mech.* **242**, 235–247.

Hunt, J. D. & Lu, S. Z. 1994 Crystallisation of eutectics, monotectics, and peritectics. In *Handbook of Crystal Growth 2. Bulk Crystal Growth, Part B: Growth Mechanisms and Dynamics* (ed. D. T. J. Hurle), pp. 1111–1166. North-Holland.

Jackson, K. A. & Hunt, J. D. 1966 Lamellar and rod eutectic growth. *Trans. Metal. Soc. AIME* **236** (8), 1129–1142.

Johnson, D. & Narayanan, R. 1998 Marangoni convection in multiple bounded fluid layers and its application to materials processing. *Phil. Trans. R. Soc. Lond.* A **356**, 885–898.

Joseph, D. D. & Renardy, Y. Y. 1993 *Fundamentals of Two-Fluid Dynamics*. Springer.

Keller, H. B. 1976 *Numerical Solution of Two-Point Boundary Value Problems*. Society for Industrial and Applied Mathematics.

Landau, L. D. & Lifshitz, E. M. 1987 *Fluid Mechanics*, *Course of Theoretical Physics*, 2nd edn., vol. 6. Butterworth-Heinemann.

Lupis, C. H. P. 1983 *Chemical Thermodynamics of Materials*. North-Holland.

McFadden, G. B. & Coriell, S. R. 2009 Onset of oscillatory convection in two liquid layers with phase change. *Phys. Fluids* **21**, 0341017.

McFadden, G. B., Coriell, S. R., Gurski, K. F. & Cotrell, D. L. 2007*a* Onset of convection in two liquid layers. *J. Res. NIST* **112**, 271–281.

McFadden, G. B., Coriell, S. R., Gurski, K. F. & Cotrell, D. L. 2007*b* Onset of convection in two liquid layers with phase change. *Phys. Fluids* **19**, 104109.

Merkwitz, M. & Hoyer, W. 1999 Liquid–liquid interfacial tension in the demixing metal systems Al-Pb and Al-In. *Z. Metallkd.* **90**, 363–370.

Nepomnyashchy, A. A., Verlarde, M. G. & Colinet, P. 2002 *Interfacial Phenomena and Convection*. Chapman & Hall/CRC.

Powell, M. J. D. 1970 A hybrid method for nonlinear equations. In *Numerical Methods for Nonlinear Algebraic Equations* (ed. P. Rabinowitz), pp. 87–114. Gordon & Breach.

Sakurai, S., Tschammer, A., Pesch, W. & Ahlers, G. 1999 Convection in the presence of a first-order phase change. *Phys. Rev.* E **60**, 539–550.

Schatz, M. F. & Neitzel, G. P. 2001 Experiments on thermocapillary instabilities. *Annu. Rev. Fluid Mech.* **33**, 93–127.

Scott, M. R. & Watts, H. A. 1977 Computational solution of linear two-point boundary-value problems via orthonormalization. *SIAM J. Numer. Anal.* **14**, 40–70.

Stöcker, C. & Ratke, L. 1999 A new 'Jackson–Hunt' model for monotectic composite growth. *J. Cryst. Growth* **203** (4), 582–593.

Stöcker, C. & Ratke, L. 2000 Monotectic composite growth with fluid flow. *J. Cryst. Growth* **212** (1), 324–333.

Tiller, W. A., Jackson, K. A., Rutter, J. W. & Chalmers, B. 1953 The redistribution of solute atoms during the solidification of metals. *Acta Metall.* **1**, 428–437.

Turner, J. S. 1973 *Buoyancy Effects in Fluids*. Cambridge University Press.

Vandevender, W. H. & Kaskell, K. H. 1970 The SLATEC mathematical subroutine library. *SIGNUM Newsl.* **17**, 16 (As of December 2009, the SLATEC library is available at http://www.netlib.org/slatec. The program SNSQ was written by K. Hiebert and is based on an algorithm of Powell 1970).